Microstructure response of concentrated suspensions to flow reversal

A. García, Y L Roht, I. Ippolito, D. Salin, G. Drazer, J P Hulin, G. Gauthier

▶ To cite this version:

A. García, Y L Roht, I. Ippolito, D. Salin, G. Drazer, et al.. Microstructure response of concentrated suspensions to flow reversal. European Physical Journal E: Soft matter and biological physics, 2025, 48 (1), pp.7. ⟨10.1140/epje/s10189-025-00472-9⟩. ⟨hal-04915455⟩

HAL Id: hal-04915455

https://hal.science/hal-04915455v1

Submitted on 27 Jan 2025

Microstructure response of concentrated suspensions to flow reversal

A. A. García[1,2*], Y. L. Roht[1*], I. Ippolito[1*], D. Salin[2*], G. Drazer[3*], J. P. Hulin[2*] and G. Gauthier[2*]

[1]Universidad de Buenos Aires, Facultad de Ingeniería, Grupo de Medios Porosos, Paseo Colón 850, 1063, Buenos Aires, Argentina.
[2]Université Paris-Saclay, CNRS, FAST, 91405 Orsay, France.
[3]Mechanical and Aerospace Engineering Department, Rutgers, The State University of New Jersey, Piscataway, NJ 08854, USA.

*Corresponding author(s). E-mail(s): aagarcia@fi.uba.ar; yroht@fi.uba.ar;

Abstract

We study experimentally at the macroscopic and microstructure scale a dense suspension of non-Brownian neutrally-buoyant spherical particles experiencing periodic reversals of flow at constant rate between parallel plates and tracked individually. We first characterize the quasi-steady state reached at the end of half periods. The volume fraction of particles increases from the walls to the center as a result of migration induced by the nonuniform strain rate. Except very close to the walls and the center, the particle pair distribution is fore-aft asymmetric with depletions of pairs in the extensional quadrants, similar to that reported for shear flows of same volume fraction as the local one. The dynamics of the periodic rearrangements occurring after each flow reversal are characterized by a microstructure tensor component. The relaxation time characterizing the reorganization increases from the walls to the center due to the inhomogeneous strain rate. On the other hand, the local accumulated strain required for this reorganization decreases with the volume fraction, like for viscosity measurements in uniform strain rate conditions. However, the variation of the microstructure with the accumulated strain is faster than that of the viscosity, showing the complementarity of the two measurements.

1 Introduction

The spatial distribution of spherical particles suspended in a viscous fluid of the same density becomes anisotropic when the suspension is subject to straining flows. This anisotropy in the shear-induced microstructure, was first proposed to explain a transient response observed in suspensions under shear reversal in Stokes flows [1, 2]. The anisotropic microstructure is typically attributed to the presence of solid contacts between neighboring particles [3], although any other irreversible interaction could in principle produce similar effects [4]. These solid contacts also account for a significant fraction of the suspension viscosity: when the flow direction is inverted, they momentarily disappear, resulting in a sharp decrease of the viscosity of the suspension [5, 6]. The particles then reorganize according to the new flow direction, solid contacts form again and the viscosity recovers its magnitude [7]. The shear-induced microstructure of non-Brownian, neutrally-buoyant suspensions in the limit of zero Reynolds number has been well characterized for steady flows with uniform shear rate [8]. In contrast, studies of the suspension microstructure in more complex flows of practical interest, such as Poiseuille channel flow, are scarse [9]. In addition, no precise characterization of the microstructure evolution of a Poiseuille flow under flow reversal is available in the literature.

Therefore, in order to improve our understanding of the suspension microstructure in flows with nonuniform shear rate and its evolution under flow reversal, we performe oscillatory channel flow experiments in which we track individual particles and determine the evolution of the microstructure. Specifically, we prepare a concentrated suspension (40% by volume) of non-colloidal, neutrally-buoyant spherical particles and make it flow at low Reynolds numbers between parallel plates. The shear-induced migration of particles produces an inhomogeneous distribution across the gap, with a particle volume fraction ϕ near the center larger than near the walls [10–12]. We compare the local microstructure obtained at different positions across the gap with results obtained in uniform shear flow at the corresponding volume fractions. We then consider the evolution of the local shear rate and microstructure after each flow reversal across the gap; their relaxation toward steady state is compared to that of the viscosity of a suspension of similar volume fraction in uniform shear flows.

2 Experiments and data analysis

2.1 Experimental setup and procedure

We use polymethylmethacrylate (PMMA) spheres of diameters $2a = 85 \pm 5\,\mu\mathrm{m}$ suspended in a solution composed of 38.8% in weight (wt) of ammonium thiocyanate (NH4SCN), 37.9%wt of glycerin and 23.3%wt of water (similar to that proposed in [13]). This solution matches both the density ($\rho = 1189\,\mathrm{Kg/m^3}$) and refractive index of the particles at temperatures around 22°C, rendering the particles neutrally buoyant and transparent. Rheological measurements with shear rates between 5 and $50\,\mathrm{s}^{-1}$ show that the fluid is Newtonian within our experimental precision and of a viscosity $\eta_f \approx 7.6\,\mathrm{mPa.s}$. The bulk volume fraction of particles is $\phi_{\mathrm{bulk}} = 0.40$. Small amounts of fluorescent dye (rhodamine 6G) and surfactant are added to the fluid, to enable the visualization of the particles and to avoid trapping air bubbles when the particles are added to the solution, respectively. The suspension is injected by a syringe pump and completely saturates a transparent channel made of PMMA with a length $L = 200\,\mathrm{mm}$ and a rectangular cross-section of width $W = 10\,\mathrm{mm}$ and gap thickness $2b = 2.00 \pm 0.05\,\mathrm{mm}$, approximating a flow between parallel plates (see schematic view in Fig. 1). In order to visualize the spherical particles, a laser beam (wavelength 532 nm) is shaped optically into a plane sheet of thickness $\approx 25\,\mu\mathrm{m}$. In the illuminated region, the dyed fluid appears bright while the particles remain dark, as seen in Fig. 1(b). The laser sheet cuts a cross section in the middle of the channel and along its length, as indicated in Fig. 1(a) together with the position of a video camera recording the experiments. The particles are detected and tracked in the videos, extracting the instantaneous positions of their centers, apparent radii and velocities.

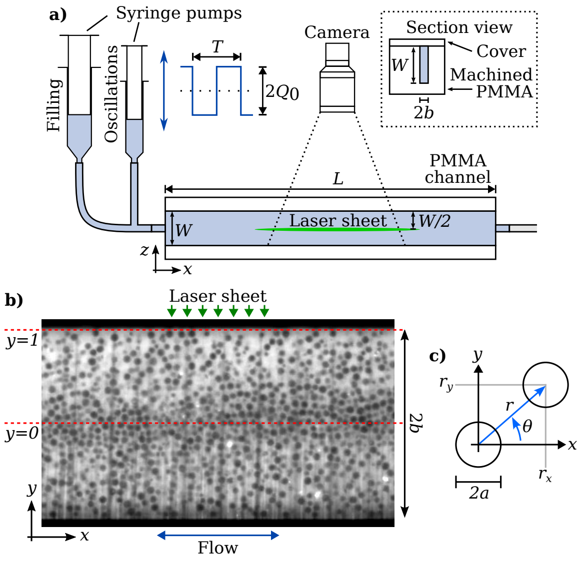

Fig. 1 a) Schematic view of the experimental setup. b) Typical image. Small region ($\approx 3\,\mathrm{mm}$ by $2\,\mathrm{mm}$) of a larger image ($\approx 19\,\mathrm{mm}$ by $2\,\mathrm{mm}$). c) Representation of a pair of particles and its relative position vector.

In each experiment, the suspension is injected slowly into an empty system to ensure reproducible initial conditions. The channel length is oriented vertically to prevent the entrapment of bubbles. Note that, during this initial flow, some shear-induced migration of the particles takes place across the gap of the channel and towards its center. After the initial injection, we start the recording, and turn on a programmable syringe pump generating square-wave variations of the flow rate, with period $T = 24\,\mathrm{s}$, as schematically shown in Fig. 1(a). Experiments with four different periods ($16\,\mathrm{s} \leq T \leq 28\,\mathrm{s}$) produced similar results; however a full study of the influence of T is not within the scope of this work. The peak absolute flow rate $Q_0 = 24\,\mathrm{mm}^3/\mathrm{s}$ corresponds to a maximum longitudinal velocity $V_{\max} = 1.59\,\mathrm{mm/s}$ at the center of the channel and corresponds to a Reynolds number $\mathrm{Re} \simeq \rho b V_{\max}/\eta_f = 0.4$. In the following, we use dimensionless variables: the coordinate across the gap is normalized by $b = 1\,\mathrm{mm}$, that is $-1 \leq y \leq 1$, the velocities by $V_{\max}$, and the time by $b/V_{\max} = 0.629\,\mathrm{s}$.

As the square-wave oscillatory flow starts, the particles continue to migrate towards the center during the first ≈ 6 oscillations. During oscillations 7 to 9, the macroscopic particle distribution is close to the steady-state ones observed in previous works, and it is only during this time range that we perform the analysis presented here. Afterwards, the flow becomes unstable with the growth of an x-periodic transverse velocity component V_y that distorts the particle distribution both along x and y [14, 15].

The particle coordinates obtained by tracking are used to compute characteristic parameters of the flow. First, the cross section captured in the images is divided into rectangular bins of equal size, where each bins covers a segment across the gap (y direction). The local volume fraction $\phi(y)$ is then estimated by counting particles inside these rectangular bins and assuming that the average value matches the bulk volume fraction $\phi_{\mathrm{bulk}} = 0.40$ [Fig. 2(a)]. The longitudinal velocity profile $V_x(y)$ is determined by averaging the displacement of individual particles inside each bin during a short time lapse. Using a numerical differentiation scheme, we also compute the strain rate $\dot{\gamma} = \partial V_x/\partial y$ across the gap [Fig. 2(b)].

Both profiles present slight asymmetries due to the sensitivity of the visualization technique to small refractive index mismatches or heterogeneities, progressively distorting the laser light as it passes through layers of spheres from top to bottom. This is specially evident in the bottom half [see Fig. 1(b)], and for this reason, all further analysis will be performed using only data from the top half of the channel ($0 < y < 1$).

In order to improve the statistics, the following averaging procedures were used. First, to take advantage of the symmetry of the flow, we divide each oscillation period in two parts, corresponding to positive and negative directions of the mean flow. Then, for the half period with positive flow, we reflect the coordinates of the particles along the flow direction such that the observed strain rate in the top region is always positive. Then, to obtain quasi-steady state results (Sec. 3.1), we perform a time average over the last 25% of each half period. Results obtained over longer times present distortions, while over shorter times, they are equivalent regarding their key features, but noisier. On the other hand, to obtain the evolution with time following a flow reversal (Sec. 3.2), we perform an ensemble average of several half periods. In both cases, the results are averaged over nine independent experiments.

2.2 Microstructure analysis

A key tool to characterize the microstructure of the suspension, especially short-range correlations of the position of the particles, is the pair distribution function (pdf). First, for each particle, we determine the relative position vector in the (x, y) plane of all the other particles [$\boldsymbol{r} = (r_x, r_y)$ in Fig. 1(c)]. After binning the (r_x, r_y) plane we define the pdf $g(r_x, r_y)$ as

$$g(r_x, r_y) = \frac{N(r_x, r_y)}{n_S\, N_1\, \Delta r_x\, \Delta r_y}, \tag{1}$$

where $\Delta r_x = \Delta r_y$ is the size of the bins, $N(r_x, r_y)$ is the number of pairs in the bin centered at (r_x, r_y), N_1 is the total number of particles in the region of interest, and $n_S = N_1/A$ is the corresponding surface number density in a region of area A. An isotropic distribution would correspond to $g = 1$ everywhere.

Since the volume fraction (and therefore the pdf) vary across the channel, the top half of the channel is divided into twelve evenly distributed thin strips along the flow direction in which the pdf is computed locally. For each particle inside a given thin strip, all pairs are taken into account, even if the second particle is located outside the strip.

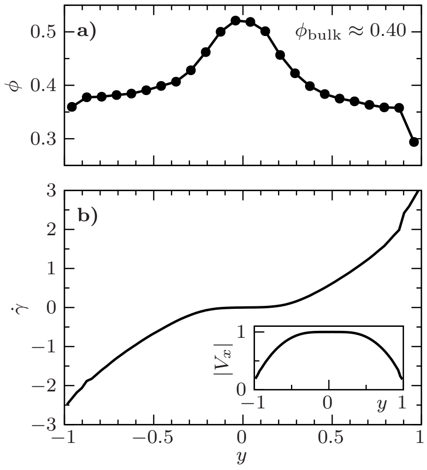

Fig. 2 Quasi-steady state (qss) profiles. a) Particle volume fraction profile $\phi(y)$. b) Strain rate, $\dot{\gamma}(y)$; inset: velocity profile $V_x(y)$.

For simplicity and improved comparison to previous results, we only consider particles located approximately in the same plane of observation. Specifically, given that spherical particles with their centers outside of the laser sheet will appear in the images as disks with smaller radii, only those with measured radius $> 0.8\,a$ are considered.

3 Experimental results

3.1 Quasi-steady state

Let us define as *quasi-steady* the state of the suspension at a long enough time after each flow reversal (a more precise definition will be discussed later), and before the next one.

Quasi-steady state (qss) profiles of the volume fraction, the velocity and the strain rate are shown in Figs. 2(a-b). The volume fraction is maximum at the center and minimum near the walls of the channel, as a result of shear-induced migration [10, 11]. Considering only the top half of the channel we can establish a unique correspondence between the position across the channel y and the local volume fraction ϕ of the suspension. Another important feature is that the velocity is maximum at the center of the channel and exhibits a blunt profile. Accordingly, the shear rate is very small in the vicinity of the center and maximum at the walls. Note that the transverse variations of the viscosity $\eta(y)$ are related to $\dot{\gamma}$, y, and the shear stress τ_{w} at the wall by:

$$\eta(y) = \tau_w \, y/\dot{\gamma}(y). \tag{2}$$

This classical macroscopic relation has been applied to suspensions where the solid phase can induce non-Newtonian behaviors [16–19]. Given the negligible inertial effects, we assume therefore that this expression is valid at all times, except during the reversal when the pump is still changing the flow direction.

Figures 3(a-c) show the pair distribution function (pdf) computed at three different positions across the gap. Note that, unlike y, the distance between particles (r_x, r_y) was made nondimensional with the radius of the particles a. In all cases, the pdf is larger in the vicinity of the circle $r = 2$ (see color scale), indicating the large probability of particles forming pairs nearly in contact. Furthermore, there is a depletion of pairs in the extensional quadrants ($r_x r_y > 0$), where the particles are separating on average. This fore-aft asymmetry can be explained by irreversible interactions between particles, generally attributed to direct solid contacts due to particle roughness [7, 20, 21]. The pdf's measured very close to the wall or near the center display different caracteristics as can be seen in the appendix (Fig. A1).

The location and thickness of the rings of high pair probability in Figs. 3(a-c) are determined quantitatively from the radial pair distribution $g(r)$, obtained like $g(r_x, r_y)$ but binning the data solely over $r = (r_x^2 + r_y^2)^{1/2}$. Everywhere, $g(r)$ displays a first peak and global maximum at $r_{\max} \approx 2.16$, with a width at half height $\Delta r_{\max} \approx 0.32$. The variations of $g(r)$ are shown in the appendix (Fig. A2).

In order to compare the fore-aft asymmetry observed in the pair distribution function with available results, we calculate the angular distribution $g(\theta)$ of pairs near contact by binning the polar angle [see Fig. 1(c)] and considering only close pairs, specifically those for which $|r - r_{\max}| \leq \Delta r_{\max}/2$ (i.e. $2 \leq r \leq 2.32$).

Figures 3(d-f) show the angular distribution of pairs near contact in the same three positions across the channel as in Figs. 3(a-c). We present separately the angular distribution of pairs above

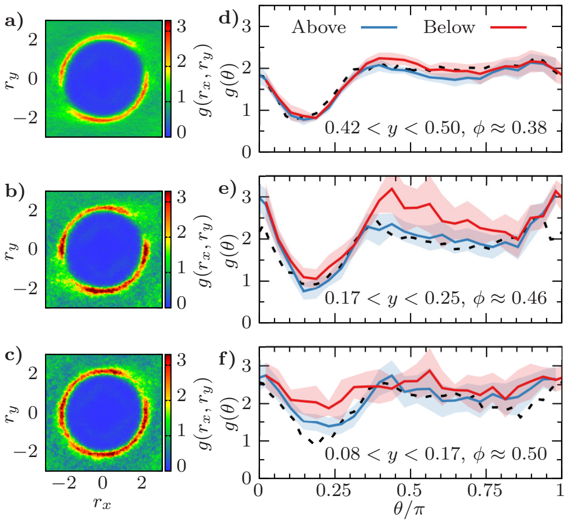

Fig. 3 Left (a,b,c): pair distribution function. Right (d,e,f): corresponding near-contact angular distributions $g(\theta)$. Each row corresponds to a different value of the distance across the channel gap and the volume fraction. The light colored bands represent the pointwise standard deviation from the nine experiments averaged. Unlike y, r_x and r_y are normalized by the particle radius a. (—): $0 < \theta < \pi$; (—): $-\pi < \theta < 0$ (plot angle shifted by π to display overlap). (- -): Couette rheometer measurements [8].

$[r_y > 0$, (—)] and below $[r_y < 0$, (—)] the reference particle, to account for possible effects of gradients of both ϕ and $\dot{\gamma}$ across the channel.

In plots (d) and (e) ($\phi \approx 0.38$ and 0.46), we observe a clear dip around $\theta = \pi/4$ corresponding to the depletion of pairs in the extensional quadrant observed in plots (a) and (b), respectively. A shallower decrease in the angular distribution is observed around $\theta = 3\pi/4$. In both cases, the measured angular distribution (particularly for $r_y > 0$) agrees well with that obtained by Blanc et al. [8] in uniform shear flows with similar volume fractions. In plot (f) ($\phi \simeq 0.50$), the depletion of pairs is less significant, particularly for $r_y < 0$. The measured angular distribution for $r_y > 0$ also agrees with that reported by Blanc et al. [8] for a similar volume fraction.

In the range of volume fractions considered, the measured angular distributions of pairs near contact are similar to those found for homogeneous shear flows at similar volume fractions, particularly for $r_y > 0$. The small discrepancies between profiles obtained above and below the reference particle may result from strain rate and volume fraction gradients present in channel flows.

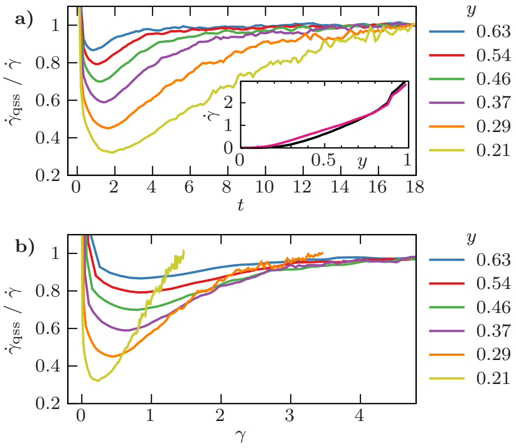

Fig. 4 Ratio $\dot{\gamma}_{\mathrm{qss}}(y)/\dot{\gamma}(y,t)$ as a function of the time normalized by $b/V_{\max}$ (a) and the local strain γ accumulated since the flow reversal (b) for different y's, i.e. different particle volume fractions. Both plots correspond to a time lapse of one half period (12 s). Inset of (a): strain rate profile before reversal (qss, —) and a short time after ($t = 1$, —).

3.2 Response to flow reversal

The results presented up to this point correspond to the quasi-steady state achieved after enough strain has been accumulated without any change of the flow direction. In this section, we study how this state is recovered after a flow reversal. A sensitive measurement of the evolution of the particle structure is that of the strain rate $\dot{\gamma}(y,t)$. In the inset of Fig. 4(a), we compare $\dot{\gamma}(y)$ at time $t = 1$ after reversal with the quasi-steady state profile $\dot{\gamma}_{\mathrm{qss}}(y)$. These curves are definitely different, meaning that the local viscosity $\eta(y)$ has changed. Note that no such dependence on time has been observed for $\phi(y)$. The value of $\eta(y)$ is related to $\dot{\gamma}$, y, and the shear stress τ_{w} at the wall by Eq. (2); we can therefore gain insights into $\eta(y)$ from the ratio $\dot{\gamma}_{\mathrm{qss}}(y)/\dot{\gamma}(y,t)$, shown in Fig. 4(a) as a function of the time t after the reversal. We observe that, except very close to the wall, the inverse of the strain rate drops down and then relaxes, with a minimum value that becomes smaller and is reached later as y decreases (and thus ϕ increases). Similar curves, but for η, were obtained in previous rheometry experiments [1, 5] and simulations [7] with uniform shear reversal: the magnitude of the drop also increases with the volume fraction ϕ. In order to separate the influences of the strain rate and the volume fraction, we use the local accumulated strain

$$\gamma(y,t) = \int_0^t \dot{\gamma}(y,t')\,\mathrm{d}t' \qquad (3)$$

to plot $\dot{\gamma}_{\mathrm{qss}}/\dot{\gamma}$ in Fig. 4(b). As y decreases and ϕ increases, the strain γ required to reach the minimum and recover the final value decreases, particularly near the center, in qualitative agreement with previous observations for the viscosity at different ϕ's [5, 7].

These transient variations of the viscosity and the strain rate can be explained by a rearrangement of the particles occurring not at a macroscopic scale [$\phi(y)$ is almost unchanged], but in the microstructure. Looking at the pdf of Figs. 3(a-c), it is expected that each reversal of the flow direction prompts the particles to reorganize and form a r_x-mirrored pdf, if enough shearing is allowed. This mirroring is equivalent to a transformation $\theta \to \pi - \theta$ in the angular distribution $g(\theta)$.

This process is visualized in the false-color maps of Fig. 5 where the evolution of $g(\theta)$ during one half period is shown for three different strips across the gap (and, therefore, different ϕ's). See also the sequence of curves $g(\theta)$ in the appendix (Fig. B3). In each map, the angles corresponding to dips of the pair probability [blue streak in (a,b), green in (c)] change to their π-complement after enough local strain γ has accumulated. As ϕ increases (from top to bottom in Fig. 5), the transition value of γ decreases, while the corresponding time duration increases, following the same trend as $\dot{\gamma}_{\mathrm{qss}}/\dot{\gamma}$ in Fig. 4. Also, the amplitude of the variations of $g(\theta)$ decreases as ϕ increases.

One observes in Figs. 5 that half maps obtained above ($0 < \theta < \pi$) and below the reference particle ($-\pi < \theta < 0$) are not identical as also noted in the steady case. This is particularly visible at the two highest mean volume fractions [cases (b) and (c)]. In these two cases, the amplitudes of the variations of g are larger above the reference particle while the value of γ corresponding to the transition is lower. This follows the global trend of variation of these two quantities with y (and the local shear rate) between strips (b) and (c).

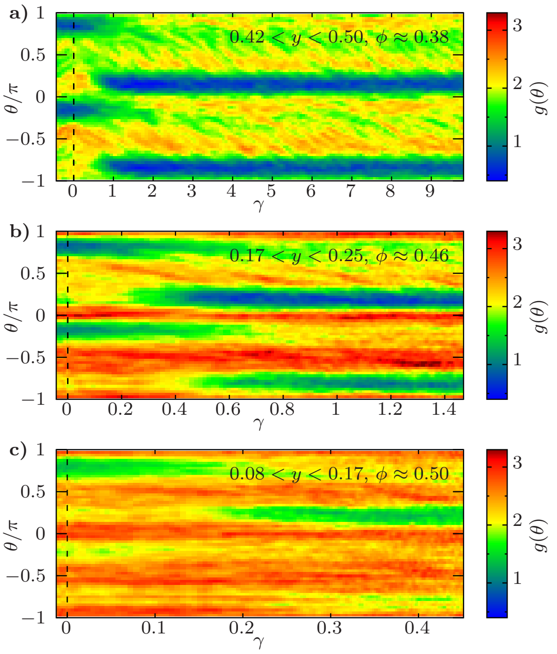

Fig. 5 Color map of the variations of the angular pair distribution in three strip across the gap of different ϕ's versus the local accumulated strain γ and the angle θ. Reversal occurs at $\gamma = 0$ and the time lapse shown by all three graphs is a half period (12 s).

In order to characterize quantitatively the time variation of the microstructure across the gap, we use, following Gillissen and Wilson [22], the xy-component of the planar projection of the microstructure tensor:

$$A^{2D}_{xy} = \left\langle \frac{r_x r_y}{r_x^2 + r_y^2} \right\rangle_{\mathrm{pairs}} = \frac{1}{2}\left\langle \sin(2\theta) \right\rangle_{\mathrm{pairs}}. \qquad (4)$$

Averaging is performed over the same pairs as for the angular distributions. This quantity is useful to characterize the mean orientation of the pairs of particles and to use its variation with the strain to characterize the evolution of the microstructure. In particular, A^{2D}_{xy} changes sign following a shear reversal.

Figure 6(a) shows the variation of A^{2D}_{xy} versus y at different times before and after the flow reversal. Consider first a flow in the $x > 0$ direction before the reversal (● symbols): A^{2D}_{xy} is positive for all y's due to the depletion of pairs for $r_x r_y < 0$, in the extensional quadrant (Figs. 3 and 5). A^{2D}_{xy} is smaller near the center because of the smaller variations of the pair function seen in Fig. 3(f). After the reversal, A^{2D}_{xy} starts to decrease toward negative values after a delay shorter near the wall ($y = 1$) than near the center ($y = 0$). The final profile when a quasi-steady state has been reached (▼),

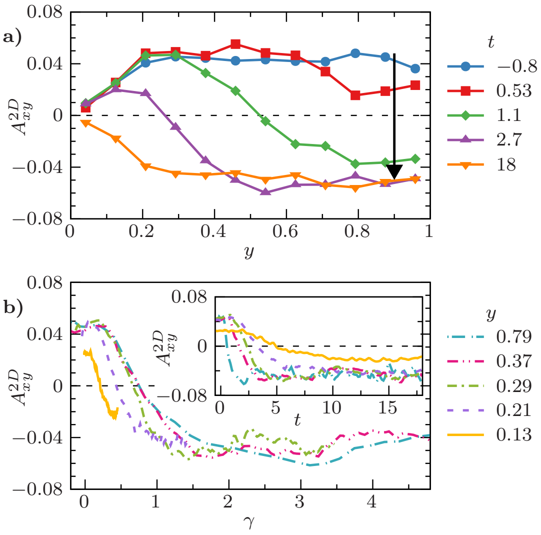

Fig. 6 a) Microstructure parameter A^{2D}_{xy} versus y at different times t since flow reversal, between -0.8 (● top) and 18 (▼ bottom). b) Evolution of A^{2D}_{xy} as a function of the local accumulated strain γ, after flow reversal at $\gamma = 0$. The curves correspond to different distances across the gap. Inset: same curves, but as a function of time.

is the opposite of the initial one, within the experimental uncertainties. Bear in mind that, in the half of the gap not shown ($-1 < y < 0$), the shear rate has the opposite sign and the microstructure evolution is similar but inverted.

Variations of A^{2D}_{xy} in selected positions across the gap are shown in Fig. 6(b) as a function of the local strain γ (main figure) and the time (inset). We see again that the transition occurs at a smaller γ toward the center where the volume fraction is larger; instead, for plots versus t, the variation is much faster near the walls where the local shear rate is larger, showing its very strong influence. For very small local deformations, $0.07 \lesssim \gamma \lesssim 0.25$ depending on the distance y, A^{2D}_{xy} remains roughly constant and, then, often drops abruptly [see also $g(\theta)$ in Fig. 5].

After flow reversal, the particles contacts disappear and start to reappear along with the microstructure asymmetry. For each strip across the gap, we determine the strain γ_0 for which $A^{2D}_{xy} = 0$, corresponding to the middle point in this process. Figure 7(a) displays γ_0 versus the local particle volume fraction ϕ of the suspension (○ symbols). As expected from homogeneous shear flows studies [5, 7], γ_0 decreases with ϕ, reflecting an increase in the rate of particles interactions. Furthermore, the critical strain γ_c for the loss of reversibility in homogeneous shear flows [23] has similar values, confirming a close connection with the microstructure reorganization.

Figure 7(b) compares the variations with γ after a shear reversal of the microstructure and the viscosity. The plot includes normalized values of $-A^{2D}_{xy}$ (—) and $1/\dot{\gamma}$ (—) for $y \approx 0.29$ ($\phi \approx 0.43$) in our work and of η (—) from rheometry measurements at a similar ϕ [5]. While $1/\dot{\gamma}$ varies in a similar way as η, $-A^{2D}_{xy}$ increases much faster. Similarly, in Fig. 7(a), the strain $\gamma_{0.5}$ needed to reach 50% of the steady viscosity is larger than γ_0 in the range of ϕ's investigated.

The viscosity of a suspension includes indeed two contributions: the hydrodynamic stress and the contact forces between particles which do not vary in the same way with the strain after a flow reversal [7]. Just after the reversal, the contact contribution disappears while the hydrodynamic one increases as the particles separate from each other. As the distance between particles increases, both the hydrodynamic contribution and the total viscosity decrease until the contact contribution increases when particles contacts form again. The fact that A^{2D}_{xy} seems to recover with less strain than the viscosity (and $1/\dot{\gamma}$) suggest that the viscosity is more sensitive than A^{2D}_{xy} to the formation of contacts, since these take place at a distance scale much smaller than the one we can observe.

4 Conclusion

We studied the microstructure developed by a suspension of spheres experiencing periodic flow reversals in the gap between parallel plates. The time between two successive reversals is large enough to assume that the suspension reaches a quasi-steady state between two reversals, except in the vicinity of the center where the strain rate is very low. Outside this region, particle pair distributions measured before each reversal (Figs. 3) correspond well to those for homogeneous shear flows of same volume fractions ϕ [8]. The distributions are anisotropic with a higher probability of pairs in near contact and a depletion of them in the extensional quadrants, marking a fore-aft asymmetry of the microstructure in the flow direction.

After a flow reversal, the parameter A^{2D}_{xy} characterizing quantitatively the organization of the

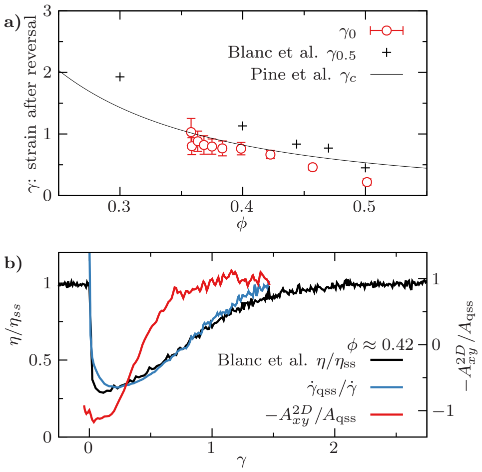

Fig. 7 a) ϕ dependence of local strains γ_0, $\gamma_{0.5}$, γ_c characterizing reorganization in different channel and Couette flows in the present work and previous ones [8, 23]. The error bars for γ_0 correspond to the standard deviation of the values calculated from each experiment individually. lb) variations with γ during and after reversal of $-A_{xy}^{2D}$ [(—), right axis], $1/\dot\gamma$ [(—), left axis] and η [(—), left axis][5]. All data are normalized to their final values.

suspension reaches a new quasi-steady-state value faster near the walls than at the center. This implies a strong influence of the local strain rate tested by plotting A_{xy}^{2D} versus the local accumulated strain γ: these curves are indeed less dispersed but relax faster as ϕ increase toward the center. This relaxation is, in particular, faster than that of the viscosity of comparable sheared suspensions after a flow reversal.

The fore-aft asymmetry can be related to the first normal stress difference [24–28], and the fact that we observe inhomogenenous relaxation times for A_{xy}^{2D} across the gap may help explain some phenomena observed during oscillations in pressure-driven flows, like instabilities [14, 15] or inverse migration [29].

The information provided by visualization methods like ours represents a promising tool to understand the rheology of spatially varying suspension flows, where local stress measurements are difficult. In particular, the components of the microstructure tensor calculated from experimental data can complement other measurements like viscosity or irreversibility thresholds: indeed, the parameter A_{xy}^{2D} essentially reflects the fore-aft asymmetry of the spatial distribution of the particles while other parameters depend in addition on hydrodynamic, contact or other forces [22, 30, 31].

In future experiments, we plan to vary the bulk volume fraction and the oscillation amplitude. Of special interest is the onset of irreversible behavior above a threshold amplitude, and its consequences for particle and fluid diffusivity [23, 32, 33].

Acknowledgements. This work was funded by the research project UBACYT 20020170100225BA. One of us (A.A.G.) is supported by a doctoral fellowship from the University of Buenos Aires and by the ADI program of the Paris-Saclay University. This research program is part of IFADyFE (Institut Franco-Argentin de Dynamique des Fluides pour l'Environnement), IRL 2027, CNRS, UBA, CONICET. We thank R. Pidoux, L. Auffray, and A. Aubertin for their help in the realization of the experimental setups and C. Manquest for characterizing the particles.

Author contribution statement

All authors contributed equally to the study discussion and manuscript writing. Material preparation, data collection and analysis were performed by AAG, under supervision of GG, II, and YLR.

Data Availability Statement. Data sets generated during the current study are available from the corresponding author on reasonable request.

Appendix A PDF on the extremes and radial distributions

The pdf's determined at different distances y across the gap display similar characteristics (Figs. 3), with the exception of those close to the wall ($0.92 < y < 1.00$) and at the center ($0.00 < y < 0.08$), shown in Fig. A1. In the first case, the high probability of pairs with $r_y \approx 0$ and negligible for pairs with $r_y \gtrsim 1$ suggests that the particles align on the wall, in agreement with the particle layering observed in the volume fraction profiles from previous works [34, 35]. In the second case, pairs remain mostly in near contact, but uniformly distributed with the angle. This latter result can be explained by the strain accumulated after flow reversal which is lower than that needed for an asymmetric organization. Note the faint secondary ring of radius $\simeq 4$ near the border of the map.

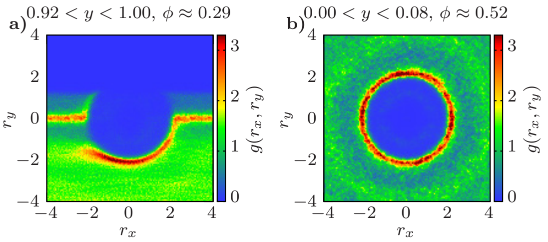

Fig. A1 Pair distribution functions $g(r_x, r_y)$ in strips located on the wall (a) and at the center (b).

Figure A2 displays the variations of the radial pair distribution $g(r)$ with the $r = \sqrt{r_x^2 + r_x^2}$ for different distances y corresponding to different volume fractions ϕ. The peak height increases with the volume fraction, implying that a larger proportion of the pairs are in near contact. The secondary peak near $r/a \simeq 4$, already visible as a faint ring in Fig. A1, appears clearly for $\phi = 0.5$ in Fig. A2.

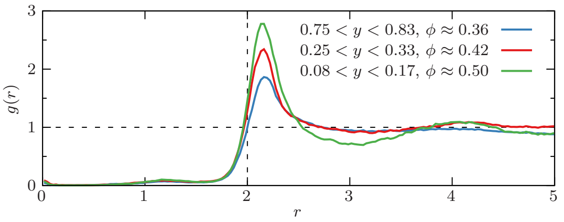

Fig. A2 Radial pair distribution $g(r)$ for three different strips across the gap.

Appendix B Time variation of the angular distribution

Figure B3 is an alternative representation of some of the data shown in Fig. 5(b). Similar observations can be made: given enough straining after reversal, the dips of minimum probability change to π-complementary angles, and for intermediate strains ($\gamma = 0.40$ and 0.55 in this case), $g(\theta)$ can be almost symmetrical with respect to $\theta = 0$.

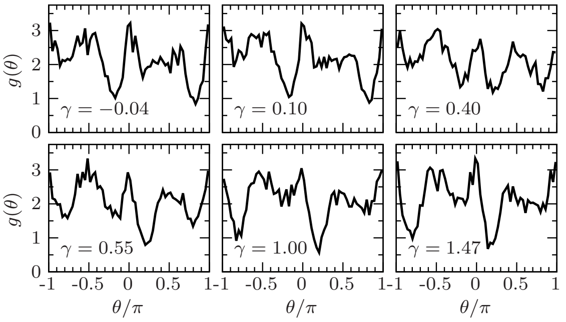

Fig. B3 Sequence of curves $g(\theta)$ for different local accumulated strains γ before and after flow reversal at $\gamma = 0$. Data obtained in strip $0.17 < y < 0.25$ corresponding to Fig. 5(b).

References

[1] Gadala-Maria, F., Acrivos, A.: Shear-Induced Structure in a Concentrated Suspension of Solid Spheres. J. Rheol. **24**(6), 799–814 (1980) https://doi.org/10.1122/1.549584

[2] Parsi, F.: Fore-and-aft asymmetry in a concentrated suspension of solid spheres. J. Rheol. **31**(8), 725–732 (1987) https://doi.org/10.1122/1.549944

[3] Lemaire, E., Blanc, F., Claudet, C., Gallier, S., Lobry, L., Peters, F.: Rheology of non-brownian suspensions: a rough contact story. Rheologica Acta **62**(5-6), 253–268 (2023) https://doi.org/10.1007/s00397-023-01394-z

[4] Drazer, G., Koplik, J., Khusid, B., Acrivos, A.: Deterministic and stochastic behaviour of non-brownian spheres in sheared suspensions. J. Fluid Mech. **460**, 307–335 (2002) https://doi.org/10.1017/S0022112002008261

[5] Blanc, F., Peters, F., Lemaire, E.: Local transient rheological behavior of concentrated suspensions. J. Rheol. **55**(4), 835–854 (2011) https://doi.org/10.1122/1.3582848

[6] Blanc, F., Peters, F., Gillissen, J.J.J., Cates, M.E., Bosio, S., Benarroche, C., Mari, R.: Rheology of dense suspensions under shear rotation. Phys. Rev. Lett. **130**, 118202 (2023) https://doi.org/10.1103/PhysRevLett.130.118202

[7] Peters, F., Ghigliotti, G., Gallier, S., Blanc,

F., Lemaire, E., Lobry, L.: Rheology of non-Brownian suspensions of rough frictional particles under shear reversal: A numerical study. J. Rheol. **60**(4), 715–732 (2016) https://doi.org/10.1122/1.4954250

[8] Blanc, F., Lemaire, E., Meunier, A., Peters, F.: Microstructure in sheared non-brownian concentrated suspensions. J. Rheol. **57**(1), 273–292 (2013) https://doi.org/10.1122/1.4766597

[9] Gao, C., Kulkarni, S.D., Morris, J.F., Gilchrist, J.F.: Direct investigation of anisotropic suspension structure in pressure-driven flow. Phys. Rev. E **81**, 041403 (2010) https://doi.org/10.1103/PhysRevE.81.041403

[10] Leighton, D., Acrivos, A.: The shear-induced migration of particles in concentrated suspensions. J. Fluid Mech. **181**, 415–439 (1987) https://doi.org/10.1017/S0022112087002155

[11] Phillips, R.J., Armstrong, R.C., Brown, R.A., Graham, A.L., Abbott, J.R.: A constitutive equation for concentrated suspensions that accounts for shear-induced particle migration. Phys. Fluids A: Fluid Dynamics **4**(1), 30–40 (1992) https://doi.org/10.1063/1.858498

[12] Rashedi, A., Sarabian, M., Firouznia, M., Roberts, D., Ovarlez, G., Hormozi, S.: Shear-induced migration and axial development of particles in channel flows of non-brownian suspensions. AIChE J. **66**(12), 17100 (2020) https://doi.org/10.1002/aic.17100

[13] Bailey, B.C., Yoda, M.: An aqueous low-viscosity density- and refractive index-matched suspension system. Exp. Fluids **35**(123), 1–3 (2003) https://doi.org/10.1007/s00348-003-0598-9

[14] Roht, Y.L., Ippolito, I., Hulin, J.P., Salin, D., Gauthier, G.: Stripes instability of an oscillating non-brownian iso-dense suspension of spheres. Europhys. Lett. **121**(5), 54002 (2018) https://doi.org/10.1209/0295-5075/121/54002

[15] Garcia, A.A., Roht, Y.L., Gauthier, G., Salin, D., Drazer, G., Hulin, J.P., Ippolito, I.: Unstable oscillatory flow of non-brownian suspensions in hele-shaw cells. Phys. Rev. Fluids **8**, 034301 (2023) https://doi.org/10.1103/PhysRevFluids.8.034301

[16] Morris, J.F., Boulay, F.: Curvilinear flows of noncolloidal suspensions: The role of normal stresses. J. Rheol. **43**(5), 1213–1237 (1999) https://doi.org/10.1122/1.551021

[17] Zarraga, I.E., Hill, D.A., Leighton Jr, D.T.: The characterization of the total stress of concentrated suspensions of noncolloidal spheres in newtonian fluids. J. Rheol. **44**(2), 185–220 (2000) https://doi.org/10.1122/1.551083

[18] Gillissen, J., Wilson, H.: Modeling sphere suspension microstructure and stress. Physical Review E **98**(3), 033119 (2018) https://doi.org/10.1103/PhysRevE.98.033119

[19] Talon, L., Salin, D.: On pressure-driven poiseuille flow with non-monotonic rheology. The European Physical Journal E **47**(8), 52 (2024) https://doi.org/10.1140/epje/s10189-024-00444-5

[20] Da Cunha, F.R., Hinch, E.J.: Shear-induced dispersion in a dilute suspension of rough spheres. J. Fluid Mech. **309**, 211–223 (1996) https://doi.org/10.1017/S0022112096001619

[21] Pham, P., Metzger, B., Butler, J.E.: Particle dispersion in sheared suspensions: Crucial role of solid-solid contacts. Phys. Fluids **27**(5), 051701 (2015) https://doi.org/10.1063/1.4919728

[22] Gillissen, J.J.J., Wilson, H.J.: Effect of normal contact forces on the stress in shear rate invariant particle suspensions. Phys. Rev. Fluids **4**, 013301 (2019) https://doi.org/10.1103/PhysRevFluids.4.013301

[23] Pine, D.J., Gollub, J.P., Brady, J.F., Leshansky, A.M.: Chaos and threshold for irreversibility in sheared suspensions. Nature **438**(7070), 997–1000 (2005) https://doi.org/10.1038/nature04380

[24] Kolli, V.G., Pollauf, E.J., Gadala-Maria, F.: Transient normal stress response in a concentrated suspension of spherical particles. J. Rheol. **46**(1), 321–334 (2002) https://doi.org/10.1122/1.1428320

[25] Sierou, A., Brady, J.F.: Rheology and microstructure in concentrated noncolloidal suspensions. J. Rheol. **46**(5), 1031–1056 (2002) https://doi.org/10.1122/1.1501925

[26] Bricker, J.M., Butler, J.E.: Correlation between stresses and microstructure in concentrated suspensions of non-brownian spheres subject to unsteady shear flows. J. Rheol. **51**(4), 735–759 (2007) https://doi.org/10.1122/1.2724886

[27] Stickel, J.J., Phillips, R.J., Powell, R.L.: A constitutive model for microstructure and total stress in particulate suspensions. J. Rheol. **50**(4), 379–413 (2006) https://doi.org/10.1122/1.2209558

[28] Seto, R., Giusteri, G.G.: Normal stress differences in dense suspensions. J. Fluid Mech. **857**, 200–215 (2018) https://doi.org/10.1017/jfm.2018.743

[29] Butler, J.E., Majors, P.D., Bonnecaze, R.T.: Observations of shear-induced particle migration for oscillatory flow of a suspension within a tube. Phys. Fluids **11**(10), 2865–2877 (1999) https://doi.org/10.1063/1.870145

[30] Gallier, S., Lemaire, E., Peters, F., Lobry, L.: Rheology of sheared suspensions of rough frictional particles. J. Fluid Mech. **757**, 514–549 (2014) https://doi.org/10.1017/jfm.2014.507

[31] Chacko, R.N., Mari, R., Fielding, S.M., Cates, M.E.: Shear reversal in dense suspensions: The challenge to fabric evolution models from simulation data. J. Fluid Mech. **847**, 700–734 (2018) https://doi.org/10.1017/jfm.2018.279

[32] Souzy, M., Pham, P., Metzger, B.: Taylor's experiment in a periodically sheared particulate suspension. Phys. Rev. Fluids **1**, 042001 (2016) https://doi.org/10.1103/PhysRevFluids.1.042001

[33] Guasto, J.S., Ross, A.S., Gollub, J.P.: Hydrodynamic irreversibility in particle suspensions with nonuniform strain. Phys. Rev. E **81**, 061401 (2010) https://doi.org/10.1103/PhysRevE.81.061401

[34] Yeo, K., Maxey, M.R.: Numerical simulations of concentrated suspensions of monodisperse particles in a poiseuille flow. J. Fluid Mech. **682**, 491–518 (2011) https://doi.org/10.1017/jfm.2011.241

[35] Snook, B., Butler, J.E., Guazzelli, E.: Dynamics of shear-induced migration of spherical particles in oscillatory pipe flow. J. Fluid Mech. **786**, 128–153 (2016) https://doi.org/10.1017/jfm.2015.645